Digital Elevation Models for topographic characterisation and flood flow modelling along low-gradient, terminal dryland rivers

Li, Jiaguang; Zhao, Yang; Bates, Paul; Neal, Jeffrey; Tooth, Stephen; Hawker, Laurence; Maffei, Carmine

Published in:
Journal of Hydrology

DOI:
10.1016/j.jhydrol.2020.125617

Publication date:
2020

Citation for published version (APA):
Li, J., Zhao, Y., Bates, P., Neal, J., Tooth, S., Hawker, L., & Maffei, C. (2020). Digital Elevation Models for topographic characterisation and flood flow modelling along low-gradient, terminal dryland rivers: A comparison of spaceborne datasets for the Río Colorado, Bolivia. *Journal of Hydrology*, [125617]. https://doi.org/10.1016/j.jhydrol.2020.125617

Accepted for Journal of Hydrology (post-print only)

Digital Elevation Models for topographic characterisation and flood flow modelling along low-gradient, terminal dryland rivers: a comparison of spaceborne datasets for the Río Colorado, Bolivia

Jiaguang Li[1*, 2], Yang Zhao[1], Paul Bates[3], Jeffrey Neal[3], Stephen Tooth[4], Laurence Hawker[3], Carmine Maffei[5]

1. Key Laboratory of Tectonics and Petroleum Resources (China University of Geosciences), Ministry of Education, Wuhan 430074, China (jiaguanglicn@yahoo.com, jiaguangli@gmail.com)

2. Key Laboratory of Theory and Technology of Petroleum Exploration and Development in Hubei Province, Wuhan 430074, China

3. School of Geographical Sciences, University of Bristol, Bristol, BS8 1SS, UK

4. Department of Geography and Earth Sciences, Aberystwyth University, Aberystwyth, SY23 3DB, UK

5. Leicester Innovation Hub, University of Leicester, University Road, LE1 7RH Leicester, UK

Abstract

Many dryland rivers are terminal systems, with small channels undergoing prominent downstream size reductions before ending on channelless floodplains, in wetlands, or at playa margins. Spaceborne Digital Elevation Models (DEMs) provide potential for assessing subtle topographic and hydrodynamic changes in these low-gradient, low-relief settings, but challenges are posed by limitations in vertical and horizontal accuracy. This study evaluates the use of different spaceborne DEMs for topographic characterisation and flood flow modelling of the low-gradient (<0.0006 m m^{-1}) Río Colorado terminal system, Bolivia. A comparison between DEM and field dGPS elevation data (1290 measurement points) reveals that the TanDEM-X DEM 12 m (TDX-12 m) has a RMSE of 0.47 m, far less than those of other frequently used spaceborne DEMs such as ALOS RTC (4.58 m) and SRTM (6.02 m). For hydrodynamic modelling, TDX-12 m data were smoothed (adaptive filter and feature-preserving DEM smoothing) and upscaled. The smoothed TDX-12 m data were mosaiced with a dGPS data-derived river path, surveyed along a reach (mean width <30 m) with a prominent downstream size decrease. The methods enabled effective de-noising of the TDX-12 m data (RMSE 0.29 m) and resulted in a high linear regression correlation coefficient (0.75). HEC-RAS 2D modelling reveals that in the selected reach, overbank flooding starts in the downstream part when discharge is <18 m^3/s, with flow initially spreading through crevasse channels and levee topographic lows. As discharge increases, flow spreads farther across the floodplain, ultimately forming connected floodplain flow in distal topographic lows. Satellite imagery and a derived water index indicate the same floodplain flow patterns as the modelling (critical success index 0.77). Wider use of DEMs based on TDX-12 m data for topographic characterization and flood flow modelling along relatively

small, low-gradient terminal dryland rivers will result in many scientific and applied benefits.

Key words: bankfull discharge, Digital Elevation Model, dryland river termini, hydrodynamic modelling, low gradient, TanDEM-X

1. Introduction

Sparsely or non-vegetated dryland river systems are receiving increasing research attention since they provide excellent modern analogues for the study of ancient (especially pre-vegetation) rock records and extraterrestrial surface environments (e.g. Grotzinger et al., 2015; Dietrich et al., 2017; Li et al., 2014a, 2020a, b; Jacobsen and Burr, 2016; Ielpi, 2018; Ielpi and Lapôtre, 2019), and also may have significance for the management of ecosystem services and flood hazards in otherwise moisture-stressed settings (Tooth, 2013; Li et al., 2018). Many low-gradient dryland rivers are terminal systems that are characterised by significant downstream decreases in cross-sectional areas and sediment transport capacity, with defined channels commonly ending on channelless plains (floodouts), in wetlands, or at playa margins (Tooth, 1999a; Tooth and McCarthy, 2007; Ralph and Hesse, 2010). Widespread overbank flooding commonly occurs during peak floods, leading to marked channel-floodplain interactions. Such interactions can have a profound influence on topographic development and flood flow dynamics, including natural levee breaching, crevasse splay development, chute cutoffs, and avulsion (e.g. Tooth, 2005; Li et al., 2014a, 2020a; Li and Bristow, 2015; Jarihani et al., 2015a, 2015b), and can also lead to the formation of less well-documented features such as topographic lobes, reforming channels, and erosion cells (Tooth, 1999a, b; Tooth et al., 2002, 2014; Li et al., 2019). In these low-relief settings, formation of such geomorphological features to a large extent is driven by subtle variations in local gradient, as this influences the distribution and rate of energy expenditure by flowing water and thus erosional and depositional patterns.

Characterisation of these subtle, interrelated topographic and hydrodynamic changes is thus essential but challenging. Relative to most research budgets, site-specific, ground-based topographic and hydrographic surveys are too time consuming and costly to constitute viable approaches, a problem that is compounded by the commonly remote locations, access problems during floods, and lack of flow gauges. Low-cost approaches to deriving DEMs using Structure-from-Motion or Google Earth imagery may provide a partial solution in some instances (e.g. Winde and Hoffmann, 2010; Prosdocimi et al., 2015) but for larger terminal dryland systems, the development of remote sensing methods for topographic characterisation and hydrodynamic modelling is typically the most practical approach, ideally in combination with targeted fieldwork.

Accurate topographic data are fundamentally important for performing hydrological modelling work, including catchment area (watershed) delineation, identification of drainage net and flow pathways, and river flood simulation (Marks and Bates, 2000; Bates, 2004, 2012; Sampson et al., 2016). Consequently, the increasing availability of Digital Elevation Model (DEM) datasets from spaceborne or airborne light detection and ranging (LiDAR) have greatly enriched data pools. For an increasing number of rivers, hydrodynamic modelling based on LiDAR data has been widely used to simulate flood patterns, flood hydrodynamics, and flood hazards (Bates, 2012; Teng et al., 2017; Milan et al., 2018, 2020; Heritage et al., 2019). Nevertheless, the expensive acquisition cost of high-resolution airborne LiDAR data limits availability on a global scale and thus potential wider application (Schumann et al., 2014; Hawker et al., 2018). As a consequence, freely available spaceborne DEMs are more widely applied in hydrological modelling (Sampson et al., 2016), including the Shuttle Radar Topography Mission (SRTM) DEM and SRTM-related products such as MERIT DEM.

Comparisons between different DEMs have been conducted in a variety of riverine settings such as in mountain regions (e.g. Czubski et al., 2013; Wang et al., 2012), tropical rainforests (Baugh et al., 2013), and deserts (e.g. Rexer and Hirt, 2014; Jarihani et al., 2015a). For example, Jarihani et al. (2015a) assessed the accuracy of three DEMs (SRTM, GDEM and the Ice, Cloud, and land Elevation Satellite (ICESat) DEM) prior to hydrodynamic modelling of a dryland river, and concluded that SRTM DEM data have higher accuracy (RMSE 3.25 m). However, the elevation change along Jarihani et al.'s (2015a) study river is up to 10 m in about 2 km (slope ~0.005 m m^{-1}), which is at least one order of magnitude higher than in many terminal dryland river systems. In these lower gradient, low relief terminal systems, high vertical and horizontal errors introduced by striping and absolute bias mean that the characterisation of subtle topographic features using commonly available DEMs remains particularly challenging (Rodriguez et al., 2006; Sampson et al., 2016; Yamazaki et al., 2012, 2017).

A potential solution to these challenges is presented by the data products from the TanDEM-X mission. Hawker et al. (2019) undertook an accuracy assessment of the freely available TanDEM-X 90 DEM for floodplain sites worldwide and concluded that it compared favourably against other spaceborne DEMs, except in forested areas (>5 m tall canopy). Careful vegetation removal and de-noising of TanDEM-X 90 m data, similar to the correction of SRTM in the MERIT DEM product, has the potential to make TanDEM-X 90 m the benchmark global DEM for floodplains. At the time of writing (mid 2020), the 12 m version of TanDEM-X (TDX-12 m) is not yet freely available, but already has proven to be advantageous for hydrodynamic modelling (Geiß et al., 2015; Schreyer et al., 2016; Archer et al., 2018). Nevertheless, although used in various settings such as mountainous (Erasmi et al., 2014; Pipaud et al., 2015), urban (Avtar et al., 2015) and estuarine (Archer et al., 2018; Pasquetti et al., 2019) areas, the application of TDX-12 m data for topographic characterisation and hydrodynamic modelling in low-gradient, low-relief, terminal dryland river systems has yet to be examined rigorously.

As a contribution to this research challenge, this study compares the utility of different spaceborne DEMs (including TDX-12 m) for topographic characterisation and flood flow modelling using HEC-RAS along the lower Río Colorado, Bolivia. The ephemeral Río Colorado terminates on the southeastern margin of Salar de Uyuni, Bolivia, the world's largest salt lake, and is subject to regular, spatially-extensive flooding. The objectives of this study are to: 1) compare the accuracy of different spaceborne DEMs in characterising the topography of this low-gradient (<0.0006 m m^{-1}), non-vegetated, terminal dryland river system; 2) develop methods to smooth and upscale the TDX-12 m data for use in hydrodynamic modelling using HEC-RAS; 3) use the hydrodynamic model results to provide insights into the spatial and temporal patterns of flooding, especially overbank flow; and 4) discuss the potential wider use of DEMs based on TDX-12 m data for improving our knowledge of the natural dynamics of low-gradient, terminal dryland rivers more generally, and the scientific and applied benefits that may accrue.

2. Study area

The Río Colorado catchment lies within the southern part of the intra-continental Altiplano basin (Fig. 1A, B), which formed as part of the Andean oceanic-continental convergent margin. The Altiplano basin is filled with Tertiary to Quaternary fluvial and lacustrine sediments and volcaniclastic deposits (Horton and Decelles, 2001; Elger et al., 2005). The Río Colorado catchment comprises upper Ordivician to Tertiary clastic sedimentary and igneous rocks, with Quaternary sediments widespread (Marshall et al., 1992; Horton and Decelles, 2001). Despite some prominent fault escarpments in the catchment (Bills et al., 1994; Baucom and Rigsby, 1999; Rigsby et al., 2005; Donselaar et al., 2013), the region has been tectonically quiescent in the late Pleistocene and Holocene.

The Altiplano has a dryland climate, with a prominent decrease in aridity index (United Nations Environment Programme, 1992) from ~0.5 in the north (dry subhumid/semiarid) to ~0.12 (arid) in the south (Lenters and Cook, 1999). The region is subject to the influence of the El Niño Southern Oscillation (ENSO) and annual precipitation totals are highly variable. In the Río Colorado catchment, annual precipitation averages ~185 mm and the 24 hour maximum daily precipitation only rarely exceeds 40 mm (Li, 2014; Li and Bristow, 2015). Annual precipitation is greatly exceeded by the annual potential evapotranspiration of 1500 mm. As a consequence, the Río Colorado is ephemeral, with river flow occurring mainly in response to thunderstorms in the austral summer (December through March) (Li et al., 2014a).

The Río Colorado flows roughly south-north, terminating on the southeastern margin of Salar de Uyuni (Fig. 1B-C). Previous studies have integrated remote sensing imagery and field observations in investigations of the channel-floodplain morphodynamics of the middle reaches and the fan-shaped lower reaches approaching the terminus (Donselaar et al., 2013; Li et al., 2014a, b, 2015, 2018, 2019, 2020a, b; Li and Bristow, 2015; van Toorenenburg et al., 2018). These studies have shown that the lower reaches of the main (trunk) channel are characterised by a prominent downstream decrease in cross-sectional area (Fig. 1D-F) and frequent (usually at least once per year) channel and overbank flood events. Field data on river sediment loads are limited, but grain-size analyses indicate that the lower Río

Colorado system is dominated by silt and clay with subordinate very fine sand (Li et al., 2015, 2020a, b). In the lowermost reaches near the terminus, channel-belt sediments are prograding over older (pre-late Holocene) lacustrine muds (Donselaar et al., 2013; Li et al., 2019). These fine-grained sediments, coupled with local salt cementation, contribute to the cohesion of bed, bank and floodplain surfaces. Normalized Difference Vegetation Index (NDVI) analysis and field observations indicate that the middle to lower reaches and terminus of the Río Colorado are essentially non-vegetated owing to the characteristically dry and saline environment (Li et al., 2015).

3. Materials and methods

For this study, a range of spaceborne satellite-derived DEMs were acquired, including freely available, frequently used DEM datasets, as well as TanDEM-X DEM (TDX-12 m) data (Table 1). These datasets were combined with high-resolution satellite imagery available from Google Earth and medium-resolution Landsat imagery (Table 2), and with differential Global Positioning System (dGPS) field surveys from the Río Colorado terminus system (Figure 1C).

3.1 Materials

3.1.1 Digital Elevation Model (DEM) data

Global or quasi-global DEMs that are freely available include Advanced Land Observing Satellite (ALOS) Radiometric Terrain Correction (ALOS RTC) (Tadono et al., 2016), ASTER GDEM (Tachikawa et al., 2011), and Shuttle Radar Topography Mission (SRTM, Farr et al., 2007). ALOS RTC is a geometrically and radiometrically terrain corrected data product derived from ALOS Phased Array type L-band Synthetic Aperture Radar (PALSAR). Addressing the effects of the side-looking geometry of SAR imagery, RTC offers RT1 products with a pixel size of 12.5 m generated from high-resolution and medium-resolution Digital Elevation Models (DEMs), as well as RT2 products generated at a 30 m resolution for all available DEMs. With its higher spatial resolution, RT1 was used in this study. The Advanced Space borne Thermal Emission and Reflection Radiometer (ASTER) global DEM (GDEM) is derived from photogrammetric processing of optical satellite imagery with artifacts and voids owing to cloud cover in the original images. SRTM is the most widely used DEM for flood modelling studies. The MERIT dataset, an error-reduced SRTM product, has been significantly improved in terms of vertical accuracy (error <2 m) (Yamazaki et al., 2017). The Land Processes Distributed Active Archive Center (LP DAAC) recently released NASADEM datasets, which were derived from original telemetry data from the Shuttle Radar Topography Mission (SRTM) (https://lpdaac.usgs.gov/news/release-nasadem-data-products/). This study includes the DEM data in the NASADEM_NC data product.

The TanDEM-X mission carried out by German AeroSpace Centre and Airbus deployed TerraSAR-X and TerraSAR-X equipped with Synthetic Aperture Radar (SAR) for Digital Elevation Measurement (TanDEM) on a global scale (Zink et al., 2014; Wessel, 2016). The mission launched a product of the global, 12-m TanDEM-X product, which covered all land surfaces with a spatial resolution of 0.4 arc seconds (~12 m). By comparison with other datasets (GNSS GCPs), the absolute vertical accuracy of TDX-12 m could be up to 2 m (Zink et al., 2014; Wessel et al., 2018; Hawker et al., 2019).

3.1.2 Satellite imagery

High-resolution (~0.5 m) satellite imagery was used to visualise the geomorphic features along the lower Río Colorado (Table 2). Two datasets (WorldView-02 and Pléiades) were used in this study. Along with other optical satellite imagery (e.g. Sentinel-2), Landsat 8 OLI imagery was used to map flooding extent. The selected Landsat imagery (05 February 2018) was based on the availability of cloud-free scenes during the rainy season (December through March).

3.1.3 dGPS data

Field dGPS data were derived from published data in van Toorenenburg et al. (2018) and van Toorenenburg (2018). The measurement system was within a <5 km radius for crevasse splays along the main channel and the accuracy was sub-centimetre (van Toorenenburg et al., 2018). High accuracy dGPS data along 8 measurement paths (see red lines in Fig. 1C) were variously oriented to characterise the longitudinal profiles and cross profiles of four crevasse splays (mean length of 1195 m, maximum length of 3080 m, minimum length of 170 m). For long-distance (up to 33-km long) measurements along the river, a vehicle-borne setup using a Trimble 5700 GNSS receiver was used (see blue line in Fig. 1C).

3.2 Methods

3.2.1 DEM accuracy assessment

High-resolution satellite imagery (Table 2) was used to evaluate the capability of spaceborne

DEM datasets to visualise some of the key geomorphological features in the study reach (e.g. channels, crevasse splays, floodplain topographic lows). We also compared the spaceborne DEMs with the field dGPS measurements. All satellite and dGPS data were registered to the same references (XY coordinate system: WGS-1984, UTM Zone 19S; vertical coordinate system: EGM2008 geoid) and were used to extract elevation data along all dGPS measurement paths. Mean error (ME), mean absolute error (MAE), and root mean square error (RMSE) have been widely used to evaluate the accuracy between dGPS values and satellite DEM datasets (Pasquetti et al., 2019; González-Moradas and Viveen, 2020) and were used in this study.

$$ME = \sum_{i=1}^{n}(H_i^* - H_i)/n \qquad (1)$$

$$MAE = \sum_{i=1}^{n}(|H_i^* - H_i|)/n \qquad (2)$$

$$RMSE = \sqrt{\frac{\sum\left(H_i^* - H_i\right)^2}{n}} \qquad (3)$$

$$LE90\% = RMSE * 90\% \qquad (4)$$

where H_i^* is satellite DEM elevation value, H_i is dGPS measurement value and n is the number of measurements. Based on this evaluation, the longitudinal long-distance dGPS data were resampled to 10 m intervals as ground-truth validation (Fig. 1C, 1290 points).

3.2.2 River construction and hydrodynamic modelling (HEC-RAS)

Deriving accurate river bathymetric depth from spaceborne DEMs for hydrodynamic modelling is challenging (Durand et al., 2008, 2010). Consequently, this study integrated dGPS data and TDX-12 m data to create accurate bathymetry for two-dimensional (2D) hydrodynamic modelling. Owing to the low gradients and the noise generated by data acquisition (Table 1), smoothing was needed to de-noise the TDX-12 m data before use in hydrodynamic modelling. Adaptive filter and feature-preserving DEM smoothing by Lindsay et al. (2019) has proven to be useful for smoothing high-resolution DEM data while still preserving crucial topographic features, and so was used to remove noise in this study. Additionally, upscaling has been used to smooth DEM data with random noise. For the TDX-12 m data, upscaling of one or two times from the original resolution was deemed suitable for further smoothing the DEM data. These effects of these combined methods on the TDX-12 m data were examined by comparing with the field dGPS data.

Based on the river parameters (river bed and banktop elevations) derived from dGPS along the main channel, a 9-km long reach with a prominent downstream decrease in cross-sectional area was selected for flood modelling. Along with the dGPS data, the river path was digitised based on high-resolution WorldView imagery (09 December 2010, WorldView-2 imagery), which was acquired for the date closest to the TDX-12 m acquisition date (Table 1). The dGPS data for the river bed were subsequently interpolated with bilinear resampling (linear across a straight line connecting two consecutive points) within the river path to create a raster with a resolution of 12 m (the same as the highest resolution of TDX-12 m). The reconstructed river path was mosaiced with the already-smoothed DEM data, and was subsequently used for 2D hydrodynamic modelling.

The HEC-RAS model developed by the US Army Corps of Engineers has proven useful for various flood inundation simulations (Brunner, 2016; Zainalfikry et al., 2020). HEC-RAS solves either the full 2D Saint Venant (eq. (5)) or 2D diffusive wave equations (eqs. (6) and (7) (Brunner, 2016).

$$\frac{\partial \zeta}{\partial x} + \frac{\partial \mathrm{p}}{\partial x} + \frac{\partial \mathrm{q}}{\partial x} = 0 \quad (5)$$

$$\frac{\partial p}{\partial t} + \frac{\partial}{\partial x}\left(\frac{p^2}{h}\right) + \frac{\partial}{\partial y}\left(\frac{pq}{h}\right) = -\frac{n^2 pg\sqrt{p^2+q^2}}{h^2} - gh\frac{\partial \zeta}{\partial x} + pf + \frac{\partial}{\rho\partial x}(h\tau_{xx}) + \frac{\partial}{\rho\partial y}(h\tau_{xy}) \quad (6)$$

$$\frac{\partial q}{\partial t} + \frac{\partial}{\partial y}\left(\frac{q^2}{h}\right) + \frac{\partial}{\partial x}\left(\frac{pq}{h}\right) = -\frac{n^2 pg\sqrt{p^2+q^2}}{h^2} - gh\frac{\partial \zeta}{\partial y} + pf + \frac{\partial}{\rho\partial y}(h\tau_{yy}) + \frac{\partial}{\rho\partial x}(h\tau_{xy}) \quad (7)$$

Owing to the complex numerical schemes, 2D diffusive wave equations (eqs. (6) and (7)) have faster calculation times and greater stability (Martins et al., 2017), and therefore were used in this study to simulate flood flows.

Meshes of 2D flow areas were established with a refined grid of 5 m × 5 m in the river and on the natural levees, and a coarse grid of 40 m × 40 m (approximately three times the resolution of the TDX data) on the floodplain. In order to conduct unsteady flow simulation, upstream and downstream boundaries were set at both ends of the selected reach. Owing to the lack of suitable gauged data, for the upstream boundary conditions, discharge was set to start at 1 m^3/s and peak at 50 m^3/s, the latter calculated from the river width-based bankfull discharge estimate model of Bjerklie (2007).

$$Q = 0.24W^{1.64} \qquad (8)$$

where Q is bankfull discharge and W is river bank width. According to daily precipitation data for the period 1980-2017 and satellite imagery in the study area, flow duration was set for eleven days with a rising period of 4 days and a decreasing period of 7 days. Normal depth with a slope of 0.0006 m m^{-1} was set for the downstream boundary condition, as based on the dGPS data. Manning's roughness coefficient ('Manning's n') was set at 0.03 for the whole model domain in accordance with the non-vegetated, fine sediment characteristics (Geleynse et al., 2010; Li et al., 2020a, b). To test model sensitivity to different Manning's roughness coefficients, we also set values of 0.02, 0.04 and 0.05.

3.2.3 Model evaluation

The hydrodynamic modelling enabled visualisation of flood flow patterns, including overbank flow paths on the more distal floodplain. In previous studies, the modified normalized difference water index (MNDWI, eq. 9) has proven useful for mapping flooding areas (Li et al., 2018), and so was used to extract flooded areas from Landsat-8 OLI imagery acquired during a rainy season (Table 2).

$$MNDWI = (\rho_{Green} - \rho_{SWIR})/(\rho_{Green} + \rho_{SWIR}) \quad (9)$$

where ρ_{Green} and ρ_{SWIR} refer to the surface reflectance values of Band 3 and Band 6 in the Landsat-8 OLI. A critical success index (CSI, eq. 10) has proven useful for evaluation of flood inundation models (see details in Stephens et al., 2014).

$$CSI = \frac{\mathrm{A}}{A+B+C} \qquad (10)$$

where A is correct flooded area (hits), B is overprediction (false alarms) and C is underprediction (misses). Therefore, CSI was used to compare the modelling results of maximum flood extent with the MNDWI-derived results.

4. Results

Accurately quantifying topography in low-gradient river systems is fundamentally important for simulating within-channel and overbank flooding processes. Our new analyses based on comparing spaceborne DEMs with field dGPS data reveal the potential provided by such datasets for enhancing topographic characterisation and flood flow modelling.

4.1 Geomorphic feature visualisation and comparison of DEM and dGPS datasets

Spaceborne DEMs have variable capabilities for visualising geomorphic features along the lower Río Colorado. Figure 3 provides an example, showing that in comparison to high-resolution satellite imagery, only TDX-12 m enables visualisation of the main channel and a crevasse channel. COPDEM also enables visualisation of the main channel but in other datasets (ALOS RTC, SRTM, MERIT, NASADEM, GDEM), these key features could barely be observed (Fig. 3). Further analysis of the DEM and dGPS data along the 8 crevasse splay measurement paths (Fig. 1C, letters a through h) shows that TDX-12 m has the smallest difference when compared with the dGPS data, with a mean value of 0.47 m for RMSE and 0.43 for LE90% (Table 3, Fig. 4). COPDEM has a mean value of 2.5 m for RMSE and NASADEM and GDEM have a similar RMSE difference (~3 m) when compared with dGPS data (Table 3, Fig. 4). ALOS RTC data (RMSE 4.58 m) and SRTM data (RMSE 6.02 m) have the greatest differences when compared with dGPS data (Table 3, Fig. 4).

Figure 5 provides a further comparison between the TDX-12 m data and the dGPS data along the 8 crevasse splay measurement paths. The plot of the mean elevation of each path with standard deviations shows that the TDX-12 m data tend to slightly overestimate elevations compared to the dGPS data but both datasets show a prominent downvalley decrease in elevation, as would be expected (Fig. 5: profiles h, c, b, a). For a single crevasse splay, the elevations of different cross profiles decrease from the proximal to the distal part, as also would be expected (Fig. 5: profiles d, e, f, g).

In addition, TDX-12 m and dGPS data (674 measurement points) from the 33-km long longitudinal profile along the main channel were compared (Table 3, Fig. 6A). Along the main channel, TDX-12 m data have a RMSE of 0.49 m. Based on the dGPS measurements of the river, the reach at 15-24 km downstream from the bridge is characterised by a prominent downstream reduction in width (~40 m to a maximum of ~15 m) and depth (~2.05 m to ~1.20 m) (Fig. 6B). This middle reach was selected for the reconstruction of the river path and thereafter incorporation into the hydrodynamic modelling domain (Fig. 6). Notably, this reach is free from human modification (e.g. no bridges or bank protection).

4.2 Smoothing and upscaling of TDX-12 m data and modelling domain construction

To remove noise from to TDX-12 m data, smoothing and upscaling were applied. The effects of these combined methods on TDX-12 m data near the main river were examined by comparing with the dGPS measurement data. The results show that these methods had a variable smoothing effect (Fig. 7A). Compared with the original TDX-12 m data, combined filters effectively removed noise (Fig. 8, Table 4). Additionally, the results of two- and three-times upscaling from the initial resolution showed that three-times upscaling enabled removal of outliers (Fig. 8C-D) while upscaling of more than three times would damage the integrity of the data. To avoid removal of elevation information by comparison with dGPS data, a combination of AF-MEC3-36 m show the lowest RMSE (0.29 m), which is 38% higher than the RMSE (0.47 m) of the original TDX-12 m data, and so this method was selected for smoothing the TDX-12 m data except outliers (Figs. 7B and 8D). Linear regression also shows that the correlation coefficient (R^2) of AF-MEC3-36 m is 0.75, compared with the R^2 of 0.26 for the original TDX-12 m data (Fig. 7A).

Smoothed TDX-12 m data mosaiced with river bathymetric data show the consistency of geomorphological characteristics in comparison with high-resolution satellite data (Fig. 9). As would be expected, a decrease in elevation is shown from the upstream to the downstream part of the reach, as well as with increased distance from the river (Fig. 9A). Also, the river decreases in width and depth from upstream to downstream (Fig. 9B: cross profiles a-b and c-d). More specifically, geomorphological features including crevasse channels, and topographic lows between crevasse splays and on the more distal floodplain can be visualised using the smoothed TDX-12 m data (Fig. 9A-C: cross profiles e-f and g-h).

4.3 Flood flow modelling

HEC-RAS model results using a Manning's roughness coefficient of 0.03 show that overbank flooding starts in the downstream part of the selected river reach at a discharge of <16 m^3/s (Table 5, Fig. 10A), with flow initially spreading through crevasse channels and topographic lows on levees. As discharge increases, the channel banks are also widely overtopped at discharges of <22 m^3/s (Table 5, Fig. 10B). As discharge increases yet further, overbank flow extends farther across the floodplain (Fig. 10C) and ultimately converges into several main flow paths in floodplain topographic lows to form connected floodplain flow (Fig. 10D). The sensitivity tests using different Manning's roughness coefficients revealed the same pattern. Regardless of the roughness coefficient, overbank flooding starts through crevasse channels and levee topographic lows when bankfull discharges are <18 m^3/s in the downstream reach and wider bank overtopping occurs at discharges <25 m^3/s (Table 5). The modelling results are validated by satellite imagery, with both Landsat OLI imagery and the MNDWI index for a February 2018 flood showing the same pattern of connected floodplain flow (Fig. 10E-F). Using quantitative assessment for the modelled results, CSI was 0.77 with low false rate (0.12), indicative of high matching with the MNDWI-derived results.

5. Interpretation and discussion

Previous studies of the Río Colorado and other low-gradient, low-energy, terminal dryland rivers have shown how local topographic and other environmental factors (e.g. soil properties) can be a key influence on erosional and depositional patterns, with spatial variations in water and sediment movement leading to a multiplicity of landforms of diverse origin, substrate type, and hydroperiod (e.g. Tooth, 1999a, b, 2005; Tooth et al., 2002; Li et al., 2019). Along the lower Río Colorado, for instance, aerial image interpretation and limited local field dGPS surveys have shown how the locations, and the rates and timescales of development of features such as crevasse splays, chute cutoffs, and erosion cells are strongly linked with local gradient changes that influence erosion and deposition during floods (Li et al., 2019, 2020a). Despite recognition of their significance, characterising such topographic and hydrodynamic changes over large areas in typically remote settings with limited access during floods has remained a major challenge. Consequently, the more widespread development of spaceborne DEMs offers considerable potential for improving our knowledge of the natural dynamics of these dryland river types, with many scientific and applied benefits, as discussed below.

5.1 Use of spaceborne DEMs for investigations of low-gradient, terminal dryland rivers

In this study of a low-gradient, non-vegetated, terminal dryland river, the comparison of different spaceborne DEMs has clearly indicated that TDX-12 m data have considerable advantages. The TDX-12 m data enable visualisation of key geomorphic features (e.g. main channel, crevasse channels) that cannot be detected using many other spaceborne DEMs (Fig. 3), and have the highest accuracy when compared with elevation data from dGPS field surveys (Fig. 4, Table 3). While the data are noisy, filtering, smoothing and upscaling techniques can improve data quality without compromising data integrity.

The Río Colorado is unusual with respect to its non-vegetated characteristics, although not unique (e.g. Ielpi, 2018; Ielpi and Lapôtre, 2019). Many other terminal dryland systems, even those located in hyperarid and arid settings, have greater (albeit patchy) riparian vegetation assemblages of grasses, shrubs, and/or trees (e.g. Tooth, 1999b, 2000), which might influence the potential wider applicability of TDX-12 m data. Comparison of TDX data between regions with different vegetation cover indicates a difference in DEM accuracy between non-vegetated and vegetated regions (Martone et al., 2018). For example, in non-vegetated Argentinian estuaries, the same level of RMSE as in this study was reported, and RMSE with dGPS data are mostly <1 m with a mean of 0.73 m (Pasquetti et al., 2019). In vegetated or sparsely vegetated regions, however, RMSE is mostly >1 m (e.g. see Table 4 in Wessel et al., 2018; Table 3 in González-Moradas and Viveen, 2020). Also, other DEMs (e.g. GDEM, SRTM) have low accuracy (RMSE up to ~20 m) in vegetated areas compared to non-vegetated terminal river systems (RMSE up to ~6 m). Even using relatively low resolution TDX-90 m data, TDX DEM data have revealed high accuracy in many landcover categories (shrubland and sparse vegetation), albeit with slightly less accuracy in short vegetation and tree covered areas (Hawker et al., 2019). Although GDEM may have low vertical errors in flat areas (Hawker et al., 2019), for the Río Colorado terminus with gradient of <0.0006 m m^{-1}, TDX-12 m data have a higher potential for characterising the topography (Table 3, Fig. 3). The accuracy differences among these DEMs indicate that TDX-12 m data are suitable for visualisation of non-vegetated or sparsely vegetated regions and applicable to hydrodynamic modelling along low-gradient, terminal dryland rivers.

5.2 Estimating bankfull discharge along small, ungauged dryland rivers

Using remote sensing approaches to estimate bankfull discharge along ungauged dryland rivers is challenging, particularly for small rivers with width <50 m (e.g. Bjerklie et al., 2005; Alsdorf et al., 2007; Tang et al., 2009). The key issue in using satellite data-derived discharge is establishing the bathymetric depth of the river channel (Birkinshaw et al., 2014). In this study, we integrated field dGPS and TDX-12 m data to construct a hydrodynamic modelling domain comprising a small river (width <50 m and depth <2 m, with both dimensions decreasing downstream) and adjacent floodplain. This modelling domain was subsequently used for estimating bankfull discharge and modelling overbank flooding. Modelling results using a Manning's roughness coefficient of 0.03 indicate that overbank flooding starts at a discharge of <16 m^3/s in the downstream reaches (river width <20 m) with flow initially dispersing through crevasse channels and low points in levees (Table 5, Fig. 10A), and that with higher discharges, overbank flooding extends farther upstream as banks are more widely overtopped (Fig. 10B-D). The sensitivity tests for different Manning's roughness coefficients revealed no essential difference in results (Table 5). The estimation of bankfull discharge at ~18 m^3/s in the downstream reaches is similar to the estimate of ~20 m^3/s using Bjerklie's (2007) model. For the river reach as a whole, widespread overbank flow occurs at a discharge of <22 m^3/s, which is >50% lower than estimates of ~50 m^3/s based on river parameters including depth and slope or width, slope and velocity (Bjerklie, 2007). These results suggest that while the Bjerklie (2007) method can still provide useful upper bound estimates of bankfull discharge in small, ungauged dryland rivers where other data do not exist (e.g. Larkin et al., 2017), there may be a tendency to overestimate bankfull discharges, especially where crevasse splays and other low points in banks or levees are widespread.

5.3 Visualising overbank flow patterns

Besides estimation of bankfull discharge, the model results are also invaluable for helping to visualise overbank flow patterns. Approaching peak flow (50 m^3/s), areas of fully connected floodplain flow with depths up to ~0.54 m become established in topographic lows distal from the main channel (Fig. 10D). Without modelling or capture of high-resolution satellite imagery around peak flow, such overbank flow patterns may be hard to recognise and appreciate, but likely have significant implications for short-term patterns of sediment and nutrient transfer and potential longer-term development of regional avulsions involving abandonment of the main channel in favour of a new course (Donselaar et al., 2013; Li et al., 2014a, 2019). Although the Río Colorado flows through a sparsely populated region, along more populated or cultivated dryland river systems, such insights may have significant implications for flood hazard assessment and floodplain zoning.

Greater insights into flood flow patterns, associated sediment transfer, and longer term channel-floodplain changes also have relevance for improved knowledge of the stratigraphy and sedimentary architecture of terminal dryland rivers. Sparsely or non-vegetated terminal dryland river systems like the Río Colorado are increasingly being cited as modern analogues to help interpret ancient (especially pre-vegetation) fluvial successions (Ielpi et al., 2018) and other fluvial sedimentary environments such as thin-bedded hydrocarbon reservoirs (van Toorenenburg et al., 2016), and also help to provide insight into extraterrestrial sedimentary environments (Matsubara et al., 2015). Although details are limited, over timescales of decades to millennia, channel-floodplain topographic and hydrodynamic changes along terminal dryland rivers likely are associated with the generation of considerable sub-surface stratigraphic complexity (Tooth, 1999b; Tooth et al., 2002; Donselaar et al., 2013). To date, most attention has focused on the impact of channel and proximal floodplain changes such as chute cutoff formation and crevasse splay development on fluvial stratigraphy and sedimentary architecture (Tooth, 2005; Li and Bristow, 2015; Li et al., 2014a, 2020a, b) but along with studies of floodplain features such as erosion cells (Li et al., 2019), the potential impact of connected floodplain flow on sediment reworking is also worthy of greater investigation. Collectively, such studies might help to provide generic, more widely applicable insights into fluvial landscape and sedimentary dynamics in low-gradient, terminal dryland rivers.

6. Conclusion

This study compared different spaceborne DEMs for topographic characterization and flood flow modelling of the low-gradient Río Colorado terminal system. The comparison between DEM and dGPS elevation data (1290 measurement points) revealed that the TanDEM-X DEM 12 m (TDX-12 m) RMSE is 0.47 m, far less than the RMSE of other frequently used DEMs such as those derived from ALOS RTC and SRTM data. As a basis for hydrodynamic modelling using HEC-RAS, TDX-12 m data were smoothed using a combination of filters (adaptive filter and feature-preserving DEM smoothing) and upscaling. The combined smoothed methods enabled effective de-noising of the TDX-12 m data (RMSE 0.29 m). The smoothed TDX-12 m data were then mosaiced with the dGPS data-derived river reach, which is characterised by a prominent downstream decrease in cross-sectional area. HEC-RAS modelling using different Manning's roughness coefficients (0.02-0.05) revealed that overbank flooding starts when discharge is <18 m^3/s in the narrower downstream reach, and occurs more widely throughout the reach at discharges <22 m^3/s. These discharges are lower than river width-based estimates of bankfull discharge, probably owing to the abundant crevasse splays and other low points in levees and bank tops. As discharge increases, comparison with satellite imagery and derived water index indicates similar overbank flow patterns, with areas of fully connected floodplain flow developing in distal topographic lows around peak stage.

This study has demonstrated the feasibility and value of using DEMs based on TDX-12 m data for enhancing knowledge of the low-gradient Río Colorado terminal system. A future research agenda should be to test the wider application of TDX-12 m data on terminal dryland systems with different hydrological, geomorphic, vegetation and soil characteristics. Demonstration of wider applicability will help to contribute to improved scientific and applied understanding, with benefits for geomorphological, hydrological, and sedimentological investigations. In an era of rapid environmental change, characterised in many dryland catchments by greater hydrological extremes and increasing human modification of hillslope, floodplain and channel characteristics, such approaches may also have benefits for improved measurement, monitoring and assessment of changes to ecosystem services and flood hazards.

Acknowledgements

This research was supported by: the National Natural Science Foundation of China (No. 41972114, No. 41602121); Wuhan Applied Foundational Frontier Project (No. 2020020601012281); the Fundamental Research Funds for the Central Universities, China University of Geosciences, Wuhan (No. CUG150616); and Open Fund (TPR-2017-01) of Key Laboratory (Ministry of Education) of Tectonics and Petroleum Resources (China University of Geosciences, Wuhan). The German Aerospace Center provided the TanDEM-X data (Grant no. GEOL2320).

References

Alsdorf, D.E., Rodriguez, E., Lettenmaier, D.P., 2007. Measuring surface water from space. Reviews of Geophysics, 45, 1-24. DOI: 10.1029/2006RG000197.

Archer, L., Neal, J.C., Bates, P.D., House, J.I., 2018. Comparing TanDEM-X Data With Frequently Used DEMs for Flood Inundation Modeling. Water Resour. Res. 54, 10,205-10,222. https://doi.org/10.1029/2018WR023688

Avtar, R., Yunus, A.P., Kraines, S., Yamamuro, M., 2015. Evaluation of DEM generation based on interferometric SAR using TanDEM-X data in Tokyo. Phys. Chem. Earth, 83–84, 166–177.

Bates, P.D., 2004. Remote sensing and flood inundation modelling. Hydrological Processes, 18(13), 2593–2597. https://doi.org/10.1002/ hyp.5649

Bates, P.D., 2012. Integrating remote sensing data with flood inundation models: How far have we got? Hydrol. Process. 26, 2515–2521. https://doi.org/10.1002/hyp.9374

Baucom, P.C., Rigsby, C.A., 1999. Climate and lake-level history of the northern Altiplano, Bolivia, as recorded in Holocene sediments of the Rio Desaguadero. J. Sediment. Res. 69, 597–611.

Baugh, C.A., Bates, P.D., Schumann, G., Trigg, M.A., 2013. SRTM vegetation removal and hydrodynamic modeling accuracy. Water Resour. Res. 49, 5276–5289.

Berry, P.A.M., Garlick, J.D., Smith, R.G., 2007. Near-global validation of the SRTM DEM using satellite radar altimetry. Remote Sensing and the Environment, 106, 17–27. https://doi.org/10.1016/j.rse.2006.07.011

Bills, B.G., de Silva, S.L., Currey, D.R., Emenger, R.S., Lillquist, K.D., Donnellan, A., Worden, B., 1994. Hydro-isostatic deflection and tectonic tilting in the central Andes: Initial results of a GPS survey of Lake Minchin shorelines. Geophys. Res. Lett. 21, 293–296. https://doi.org/10.1029/93GL03544

Birkinshaw, S.J., Moore, P., Kilsby, C.G., O'Donnell, G.M., Hardy, A.J., Berry, P.A.M., 2014. Daily discharge estimation at ungauged river sites using remote sensing. Hydrol. Process. 28, 1043–1054. https://doi.org/10.1002/hyp.9647

Bjerklie, D.M., 2007. Estimating the bankfull velocity and discharge for rivers using remotely sensed river morphology information. J. Hydrol. 341, 144–155. https://doi.org/10.1016/j.jhydrol.2007.04.011

Bjerklie, D.M., Moller, D., Smith, L.C., Dingman, S.L., 2005. Estimating discharge in rivers using remotely sensed hydraulic information. J. Hydrol. 309, 191–209. https://doi.org/10.1016/j.jhydrol.2004.11.022

Brunner, G.W., 2016. HEC-RAS River Analysis System, 2D Modeling User's Manual Version

5.0. Davis, CA.

Czubski, K., Kozak, J., Kolecka, N., 2013. Accuracy of SRTM-X and ASTER elevation data and its influence on topographical and hydrological modeling: Case study of the Pieniny Mts. in Poland. Int. J. Geoinformatics 9, 7–14.

Dietrich, W.E., Palucis, M.C., Williams, R.M.E., Lewis, K.W., Rivera-Hernandez, F., and Sumner, D.Y., 2017, Fluvial Gravels on Mars: Analysis and Implications, in Tsutsumi, D., and Laronne, J.B., eds., Gravel-Bed Rivers: Processes and Disasters: Hoboken, New Jersey, USA, John Wiley & Sons Ltd., p. 755–784, https://doi .org/10.1002/9781118971437.ch28.

Donselaar, M.E., Gozalo, M.C.C., Moyano, S., 2013. Avulsion processes at the terminus of low-gradient semi-arid fluvial systems: Lessons from the Río Colorado, Altiplano endorheic basin, Bolivia. Sediment. Geol. 283, 1–14. https://doi.org/10.1016/j.sedgeo.2012.10.007

Durand, M., Andreadis, K.M., Alsdorf, D.E., Lettenmaier, D.P., Moller, D., Wilson, M., 2008. Estimation of bathymetric depth and slope from data assimilation of swath altimetry into a hydrodynamic model. Geophysical Research Letters 35: DOI: 10.1029/2008GL034150.

Durand, M., Rodriguez, E., Alsdorf, D.E., Trigg, M., 2010. Estimating River Depth FromRemote Sensing Swath Interferometry Measurements ofRiverHeight, Slope, and Width. IEEE J. Sel. Topics Appl. Earth Observ. 3, 20–31.

Elger, K., Oncken, O., Glodny, J., 2005. Plateau-style accumulation of deformation: Southern Altiplano. Tectonics 24, n/a-n/a. https://doi.org/10.1029/2004TC001675

Erasmi, S., Rosenbauer, R., Buchbach, R., Busche, T., Rutishauser, S., 2014. Evaluating the quality and accuracy of TanDEM-X digital elevation models at archaeological sites in the

Cilician Plain, Turkey. Remote Sens. 6, 9475–9493.

Farr, T., Rosen, P., Caro, E., Crippen, R., Duren, R., Hensley, S., Kobrick, M., Paller, M., Rodríguez, E., Roth, L., Seal, D., Shaffer, S., Shimada, K., Umland, J., Werner, M., Oskin, M., Burbank, D., Alsdorf, D., 2007. The shuttle radar topography mission. Rev. Geophys. 45, 536. https://doi.org/10.1029/2005RG000183. RG2004.

Geiß, C., Wurm, M., Breunig, M., Felbier, A., Taubenböck, H., 2015. Normalization of TanDEM-X DSM data in urban environments with morphological filters. IEEE Trans. Geosci. Remote Sens. 53, 4348–4362. https://doi.org/10.1109/TGRS.2015.2396195

Geleynse, N., Storms, J.E.A., Stive, M.J.F., Jagers, H.R.A., Walstra, D.J.R., 2010. Modeling of a mixed-load fluvio-deltaic system. Geophysical Research Letters, 37(5), 1–7. https://doi.org/10.1029/2009GL042000

González-Moradas, M. del R., Viveen, W., 2020. Evaluation of ASTER GDEM2, SRTMv3.0, ALOS AW3D30 and TanDEM-X DEMs for the Peruvian Andes against highly accurate GNSS ground control points and geomorphological-hydrological metrics. Remote Sens. Environ. 237, 111509. https://doi.org/10.1016/J.RSE.2019.111509

Grotzinger, J.P., Gupta, S., Malin, M.C., Rubin, D.M., Schieber, J., Siebach, K., et al., 2015. Deposition, exhumation, and paleoclimate of an ancient lake deposit, Gale crater, Mars. Science, 350(6257), aac7575. https://doi.org/10.1126/science.aac7575

Hawker, L., Bates, P., Neal, J., Rougier, J., 2018. Perspectives on Digital Elevation Model (DEM) Simulation for Flood Modeling in the Absence of a High-Accuracy Open Access Global DEM. Front. Earth Sci. 6, 1–9. https://doi.org/10.3389/feart.2018.00233

Hawker, L., Neal, J., Bates, P., 2019. Accuracy assessment of the TanDEM-X 90 Digital Elevation Model for selected floodplain sites. Remote Sens. Environ. 232.

https://doi.org/10.1016/j.rse.2019.111319

Heritage, G., Entwistle, N., Milan, D., Tooth, S., 2019. Quantifying and contextualising cyclone-driven, extreme flood magnitudes in bedrock-influenced dryland rivers. Adv. Water Resour. 123, 145–159. https://doi.org/S0309170818303828

Horton, B.K., Decelles, P.G., 2001. Modern and ancient fluvial megafans in the foreland basin system of the central Andes, southern Bolivia: implications for drainage network evolution in fold-thrust belts. Basin Res. 13, 43–63.

Ielpi, A., 2018. Morphodynamics of meandering streams devoid of plant life: Amargosa River, Death Valley, California. GSA Bull. 131, 782–802. https://doi.org/10.1130/B31960.1

Ielpi, A., Lapôtre, M.G.A., 2019. A tenfold slowdown in river meander migration driven by plant life. Nat. Geosci. https://doi.org/10.1038/s41561-019-0491-7

Ielpi, A., Fralick, P., Ventra, D., Ghinassi, M., Lebeau, L. E., Marconato, A., et al., 2018. Fluvial floodplains prior to greening of the continents: stratigraphic record, geodynamic setting, and modern analogues. Sedimentary Geology, 372, 140-172.

Jacobsen, R.E., Burr, D.M., 2016. Greater contrast in Martian hydrological history from more accurate estimates of paleodischarge. Geophys. Res. Lett. 43, 8903–8911. https://doi.org/10.1002/2016GL070535

Jarihani, A.A., Callow, J.N., McVicar, T.R., Van Niel, T.G., Larsen, J.R., 2015a. Satellite-derived Digital Elevation Model (DEM) selection, preparation and correction for hydrodynamic modelling in large, low-gradient and data-sparse catchments. J. Hydrol. 524, 489–506. https://doi.org/10.1016/j.jhydrol.2015.02.049

Jarihani, A.A., Larsen, J.R., Callow, J.N., McVicar, T.R., Johansen, K., 2015b. Where does all the water go? Partitioning water transmission losses in a data-sparse, multi-channel and low-gradient dryland river system using modelling and remote sensing. J. Hydrol. 529, 1511–1529. https://doi.org/10.1016/j.jhydrol.2015.08.030

Larkin, Z.T., Ralph, T.J., Tooth, S., McCarthy, T.S., 2017. The interplay between extrinsic and intrinsic controls in determining floodplain wetland characteristics in the South African drylands. Earth Surface Processes and Landforms, 42, 1092–1109. https://doi.org/10.1002/esp.4075.

Lenters, J.D., Cook, K.H., 1999. Summertime Precipitation Variability over South America: Role of the Large-Scale Circulation. Mon. Weather Rev. 127, 409–431.

Li, J., 2014. Terminal fluvial systems in a semi-arid endorheic basin, Salar de Uyuni (Bolivia). Uitgeverij BOX Press, ’s-Hertogenbosch, The Netherlands.

Li, J., Bristow, C.S., 2015. Crevasse splay morphodynamics in a dryland river terminus: Río Colorado in Salar de Uyuni Bolivia. Quat. Int. 377, 71–82. https://doi.org/10.1016/j.quaint.2014.11.066

Li, J., Donselaar, M.E., Hosseini Aria, S.E., Koenders, R., Oyen, A.M., 2014a. Landsat imagery-based visualization of the geomorphological development at the terminus of a dryland river system. Quat. Int. 352, 100–110. https://doi.org/10.1016/j.quaint.2014.06.041

Li, J., Grenfell, M.C., Wei, H., Tooth, S., Ngiem, S., 2020a. Chute cutoff-driven abandonment and sedimentation of meander bends along a fine-grained, non-vegetated, ephemeral river on the Bolivian Altiplano, Geomorphology, 350, 106917. https://10.1016/j.geomorph.2019.106917).

Li, J., Luthi, S.M., Donselaar, M.E., Weltje, G.J., Prins, M.A., Bloemsma, M.R., 2015. An ephemeral meandering river system: Sediment dispersal processes in the Río Colorado, Southern Altiplano Plateau, Bolivia. Zeitschrift für Geomorphol. 59, 301–317.

https://doi.org/10.1127/zfg/2014/0155

Li, J., Menenti, M., Mousivand, A., Luthi, S.M., 2014b. Non-vegetated playa morphodynamics using multi-temporal landsat imagery in a semi-arid endorheic basin: Salar de Uyuni, Bolivia. Remote Sens. 6, 10131–10151. https://doi.org/10.3390/rs61010131

Li, J., Tooth, S., Yao, G., 2019. Cascades of sub-decadal, channel-floodplain changes in low-gradient, non-vegetated reaches near a dryland river terminus: Salar de Uyuni, Bolivia. Earth Surf. Process. Landforms 44, 490–506. https://doi.org/10.1002/esp.4512

Li, J., Vandenberghe, J., Mountney, N.P., Luthi, S.M., 2020b. Grain-size variability of point-bar deposits from a fine-grained dryland river terminus, Southern Altiplano, Bolivia. Sediment. Geol. 403, 105663. https://doi.org/10.1016/j.sedgeo.2020.105663

Li, J., Yang, X., Maffei, C., Tooth, S., Yao, G., 2018. Applying independent component analysis on Sentinel-2 imagery to characterize geomorphological responses to an extreme flood event near the non-vegetated Río Colorado terminus, Salar de Uyuni, Bolivia. Remote Sens. 10, 725. https://doi.org/10.3390/rs10050725

Lindsay, J.B., Francioni, A., Cockburn, J.M.H., 2019. LiDAR DEM smoothing and the preservation of drainage features. Remote Sens. 11, 17–19. https://doi.org/10.3390/rs11161926

Marks, K., Bates, P.D., 2000. Integration of high resolution topographic data with floodplain flow models. Hydrological Processes, 14(11-12), 2109–2122. https://doi.org/10.1002/1099-1085(20000815/30)14:11/12<2109::AID-HYP58>3.0.CO;2-1

Marshall, L.G., Swisher III, C.C., Lavenu, A., Hoffstetter, R., Curtis, G.H., 1992. Geochronology of the mammal-bearing late Cenozoic on the northern Altiplano, Bolivia.

J. South Am. Earth Sci. 5, 1–19.

Martins, R., Leandro, J., Chen, A., Djordjević, S., 2017. A comparison of three dual drainage models: shallow water vs local inertial vs diffusive wave. J. Hydroinformatics 19, 331–348.

Martone, M., Rizzoli, P., Wecklich, C., Gonzalez, C., Bueso-Bello, J.-L., Valdo, P., et al., 2018. The global forest/non-forest map from TanDEM-X interferometric SAR data. Remote Sensing of Environment, 205, 352–373. https://doi.org/10.1016/j.rse.2017.12.002

Matsubara, Y., Howard, A.D., Burr, D.M., Williams, R.M.E., Dietrich, W.E., Moore, J.M., 2015. River meandering on Earth and Mars: A comparative study of Aeolis Dorsa meanders, Mars and possible terrestrial analogs of the Usuktuk River, AK, and the Quinn River, NV. Geomorphology 240, 102–120. https://doi.org/10.1016/j.geomorph.2014.08.031

Milan, D., Heritage, G., Tooth, S., Entwistle, N., 2018. Morphodynamics of bedrock-influenced dryland rivers during extreme floods: Insights from the Kruger National Park, South Africa. GSA Bull. 1–17. https://doi.org/10.1130/B31839.1

Milan, D.J., Tooth, S., Heritage, G.L., 2020. Topographic, hydraulic, and vegetative controls on bar and island development in mixed bedrock-alluvial, multichanneled, dryland rivers. Water Resour. Res. 56, 1–23. https://doi.org/10.1029/2019WR026101

Pasquetti, F., Bini, M., Ciampalini, A., 2019. Accuracy of the TanDEM-X Digital Elevation Model for Coastal Geomorphological Studies in Patagonia (South Argentina). Remote Sens. 11, 1767. https://doi.org/10.3390/rs11151767

Placzek, C.J., Quade, J., Patchett, P.J., 2011. Isotopic tracers of paleohydrologic change in large lakes of the Bolivian Altiplano. Quat. Res. 75, 231–244.

Prosdocimi, M., Calligaro, S., Sofia, G., Dalla Fontana, G., Tarolli, P., 2015. Bank erosion in agricultural drainage networks: New challenges from structure-from-motion photogrammetry for post-event analysis. Earth Surf. Process. Landforms 40, 1891–1906. https://doi.org/10.1002/esp.3767

Ralph, T.J., Hesse, P.P., 2010. Downstream hydrogeomorphic changes along the Macquarie River, southeastern Australia, leading to channel breakdown and floodplain wetlands. Geomorphology 118, 48–64. https://doi.org/10.1016/j.geomorph.2009.12.007

Rexer, M., Hirt, C., 2014. Comparison of free high resolution digital elevation data sets (ASTER GDEM2, SRTM v2.1/v4.1) and validation against accurate heights from the Australian National Gravity Database. Aust. J. Earth Sci. 61, 213–226.

Rigsby, C.A., Bradbury, J.P., Baker, P.A., Rollins, S.M., Warren, M.R., 2005. Late Quaternary palaeolakes, rivers, and wetlands on the Bolivian Altiplano and their palaeoclimatic implications. J. Quat. Sci. 20, 671–691. https://doi.org/10.1002/jqs.986

Rizzoli, P., Martone, M., Gonzalez, C., Wecklich, C., Borla Tridon, D., Bräutigam, B., Bachmann, M., Schulze, D., Fritz, T., Huber, M., Wessel, B., Krieger, G., Zink, M., Moreira, A., 2017. Generation and performance assessment of the global TanDEM-X digital elevation model. ISPRS J. Photogramm. Remote Sens. 132, 119–139.

Rodriguez, E., Morris, C.S., Belz, J.E., 2006. A global assessment of the SRTM performance. Photogramm. Eng. Remote Sens. 72, 249–260.

Sampson, C.C., Smith, A.M., Bates, P.D., Neal, J.C., Trigg, M.A., 2016. Perspectives on open access high resolution Digital Elevation Models to produce global flood hazard layers. Frontiers in Earth Science, 3(85). https://doi.org/10.3389/feart.2015.00085

Schreyer, J., Geiß, C., Lakes, T., 2016. TanDEM-X for Large-Area Modeling of Urban Vegetation Height: Evidence from Berlin, Germany. IEEE J. Sel. Top. Appl. Earth Obs.

Remote Sens. 9, 1876–1887. https://doi.org/10.1109/JSTARS.2015.2508660

Schumann, G. J. P., Bates, P. D., Neal, J. C., & Andreadis, K. M., 2014. Technology: Fight floods on a global scale. Nature, 507 (7491), 169. https:// doi.org/10.1038/507169e

Stephens, E., Schumann, G., Bates, P., 2014. Problems with binary pattern measures for flood model evaluation. Hydrol. Process. 28, 4928–4937. https://doi.org/10.1002/hyp.9979

Tachikawa, T., Kaku, M., Iwasaki, A., 2011. ASTER GDEM version 2 validation report. Report to the ASTER GDEM version 2 validation Team. https://ssl.jspacesystems.or.

Tadono, T., Nagai, H., Ishida, H., Oda, F., Naito, S., Minakawa, K., Iwamoto, H., 2016. Generation of the 30 m-mesh global digital surface model generated by ALOS PRISM. In: The International Archives of the Photogrammetry, Remote Sensing and Spatial Information Sciences, ISPRS, XLI-B4, pp. 157–162.

Takaku, J., Tadono, T., Tsutsui, K., 2014. Generation of high resolution global DSM from ALOS PRISM. Int. Arch. Photogramm. Remote. Sens. Spat. Inf. Sci., 40, 243.

Tang, Q., Gao, H., Lu, H., Lettenmaier, D.P., 2009. Remote sensing: hydrology. Progress in Physical Geography 33, 490–509.

Teng, J., Jakeman, A.J., Vaze, J., Croke, B.F.W., Dutta, D., Kim, S., 2017. Flood inundation modelling: A review of methods, recent advances and uncertainty analysis. Environ. Model. Softw. 90, 201–216. https://doi.org/10.1016/j.envsoft.2017.01.006

Tooth, S, 1999a. Floodouts in central Australia, in: Miller, A.J., Gupta, A. (Eds.), Varieties of Fluvial Form. Wiley, Chichester, pp. 219–247.

Tooth, S., 1999b. Downstream changes in floodplain character on the Northern Plains of arid central Australia, in: Smith, N.D., Rogers, J. (Eds.), Fluvial Sedimentology VI.

International Association of Sedimentologists, Special Publication No. 28, Blackwell Oxford, UK, pp. 93–112.

Tooth, S., 2000. Downstream changes in dryland river channels: the Northern Plains of arid central Australia. Geomorphology, 34, 33-54.

Tooth, S., 2005. Splay formation along the lower reaches of ephemeral rivers on the Northern Plains of arid central Australia. Journal of Sedimentary Research, 75, 634-647. https://doi.org/10.2110/jsr.2005.052

Tooth, S., 2013. Dryland fluvial environments: assessing distinctiveness and diversity from a global perspective, in: Shroder, J. (Editor in Chief) and Wohl, E.E. (Ed.), Treatise on Geomorphology. Academic Press, San Diego, CA, Vol. 9, Fluvial Geomorphology, pp. 612-644 (DOI: 10.1016/B978-0-12-374739-6.00257-8).

Tooth, S., McCarthy, T.S., 2007. Wetlands in drylands: geomorphological and sedimentological characteristics, with emphasis on examples from southern Africa. Prog. Phys. Geogr. 31, 3–41. https://doi.org/10.1177/0309133307073879

Tooth, S., McCarthy, T.S., Rodnight, H., Keen-Zebert, A., Rowberry, M.D. and Brandt, D., 2014. Late Holocene development of a major fluvial discontinuity in floodplain wetlands of the Blood River, eastern South Africa. Geomorphology, 205, 128-141. https://doi.org/10.1016/j.geomorph.2011.12.045

Tooth, S., McCarthy, T.S., Hancox, P.J., Brandt, D., Buckley, K., Nortje, E., McQuade, S., 2002. The geomorphology of the Nyl River and floodplain in the semi-arid Northern Province, South Africa. South African Geographical Journal 84, 226-237.

United Nations Environment Programme (UNEP). 1992. World Atlas of Desertification. Edward Arnold: London.

Van Toorenenburg, K.A., 2018. The Key Role of Crevasse Splays in Prograding River Systems - Analysis of Evolving Floodplain Accommodation and its Implications for Architecture and Reservoir Potential. Published Doctorate thesis. Delft University of Technology, Delft, The Netherlands, 978-94-6366-084-6 pp. 122.

van Toorenenburg, K.A., Donselaar, M.E., Weltje, G.J., 2018. The life cycle of crevasse splays as a key mechanism in the aggradation of alluvial ridges and river avulsion. Earth Surf. Process. Landforms 43, 2409–2420. https://doi.org/10.1002/esp.4404

Wang, W., Yang, X., Yao, T., 2012. Evaluation of ASTER GDEM and SRTM and their suitability in hydraulic modelling of a glacial lake outburst flood in southeast Tibet. Hydrol. Process. 26, 213–225.

Wessel, B., 2016. TanDEM-X ground segment DEM products specification document, Earth observation center, DLR, Oberpfaffenhofen, Germany.

Wessel, B., Huber, M., Wohlfart, C., Marschalk, U., Kosmann, D., Roth, A., 2018. Accuracy assessment of the global TanDEM-X digital elevation model with GPS data. ISPRS J. Photogramm. Remote Sens. 139, 171–182.

Winde, F., Hoffmann, E., 2010. Generating high-resolution digital elevation models for wetland research using Google EarthTM imagery - An example from South Africa. Water SA 36, 53–68.

Yamazaki, D., Baugh, C. A., Bates, P. D., Kanae, S., Alsdorf, D. E., Oki, T., 2012. Adjustment of a spaceborne DEM for use in floodplain hydrodynamic modeling. Journal of Hydrology, 436-437, 81–91. https://doi.org/10.1016/j.jhydrol.2012.02.045

Yamazaki, D., Ikeshima, D., Tawatari, R., Yamaguchi, T., O'Loughlin, F., Neal, J.C., Sampson, C.C., Kanae, S., Bates, P.D., 2017. A high-accuracy map of global terrain elevations.

Geophys. Res. Lett. 44 (11), 5844–5853.

Zainalfikry, M.K., Ab Ghani, A., Zakaria, N.A. Chan, N.W., 2020. HEC-RAS One-dimensional hydrodynamic modelling for recent major flood events in Pahang River. In: Mohamed Nazri F. (eds) Proceedings of AICCE'19. AICCE 2019. Lecture Notes in Civil Engineering, Vol 53. Springer, Cham, Chapter 84, pp. 1099-1115.

Zink, M., Bachmann, M., Brautigam, B., Fritz, T., Hajnsek, I., Moreira, A., Wessel, B., Krieger, G., 2014. TanDEM-X: the new global DEM takes shape. IEEE Geoscience and Remote Sensing Magazine 2, 8–23.

Figure captions

Fig. 1 Location and characteristics of the lower Río Colorado catchment and study reach: (A) the Altiplano region in South America (modified after Placzek et al., 2011); (B) map of the Altiplano showing the location of Salar de Uyuni and the Río Colorado in the southeast (modified after Placzek et al., 2011); (C) the lower reaches of the Río Colorado approaching the southeastern margin of Salar de Uyuni. The blue line is the main (trunk) channel of the Río Colorado and the dGPS measurement path along the trunk channel, while the red lines (a-h) indicate the paths of dGPS measurements along crevasse splays (see Figures 5 and 7). The asterisks with capital letters indicate the locations of the photos in parts E and F. The rectangle and polygon indicate the areas of Figures 4 and 8, respectively, with the polygon indicating the river reach and adjacent floodplain selected for hydrodynamic modelling; (D) downstream reduction in cross-sectional area along the Río Colorado (blue line in C, red dot indicating the starting point at the bridge crossing; modified from Donselaar et al., 2013); (E) photograph of the upstream reach of the Río Colorado (~50 m wide); (F) photograph of the downstream reach of the Río Colorado (~15 m wide).

Fig. 2 Flow chart showing the data processing steps undertaken in this study.

Fig. 3 Comparison of geomorphic feature detection using high-resolution satellite imagery (Pléiades, from Google Earth) and spaceborne DEMs.

Fig. 4 Histograms of difference in elevation between DEM datasets and dGPS data. (A) TDX-

12 m; (B) COPDEM; (C) ALOS RTC; (D) SRTM; (E) MERIT; (F) NASADEM; (G) GDEM.

Fig. 5 Comparison of TDX-12 m and dGPS data from eight measurement paths along crevasse splays adjacent to the main channel (see Fig. 1C, a through h). Paths a, b and h were undertaken along the splay channel beds, while paths c-g are cross-channel transects. The dotted line is the 1:1 correspondence line.

Fig. 6 (A) Comparison of TDX-12 m data and dGPS measurements of river bed and bank elevations along the lower Río Colorado (see the blue line in Fig. 1C for the river bed); (B) detail of the dGPS measurements of river width and depth in a selected reach from 15-24 km downstream.

Fig. 7 Example of various smoothing methods applied to the longitudinal profile of a crevasse splay (see Fig. 1C, path a): (A) comparison of a combination of smoothing methods for path a. Smoothing methods include: AF = adaptive filter; FP = feature-preserving DEM smoothing with default settings; MEC3 = maximum elevation change of 3 for feature preservation filter. 12 m, 24 m and 36 m are upscaling values. Dashed lines of linear regression indicate the original TDX-12 m data and the selected method (AF-MEC3-36m); (B) statistics of RMSE values between smoothed results and dGPS data.

Fig. 8 Original data and post-processing TDX-12 m data: (A) original data; (B) adaptive filter; (C) AD-MEC3; (D) AD-MEC3-36m.

Fig. 9 Reconstructed hydrodynamic modelling domain: (A) selected reach of the river. Gridded areas are the modelling domain for this study, with lines indicating the upstream and downstream boundaries. Lines labelled a through j indicate the locations of profiles in B-D; (B) elevation profiles within the reconstructed modelling domain (see A for locations); (C) location of profile across a crevasse channel adjacent to the trunk channel; (D) location of a profile across a topographic low adjacent to the trunk channel and between two active crevasse splays.

Fig. 10 Overbank flow patterns along the selected reach of Río Colorado with its marked downstream reduction in channel cross-sectional area: (A)-(D): modelling results at four different discharges; (E) false-color composite (Bands 7, 5 and 1 of Landsat 8 on 05 Feb 2018). CS = crevasse splay; TL = topographic low; (F) modified normalized difference water index (MNDWI) results, with the white areas indicating flooded areas.

Table captions

Table 1 Spaceborne DEM datasets used in this study (ALOS RTC refers to Radiometric Terrain Correction).

Table 2 Information regarding the high- and medium-resolution satellite imagery used in this study

Table 3 Statistics of difference between dGPS data and DEM datasets for 8 overbank measurement paths (ME is mean error, MAE is mean absolute error, RMSE is root mean square error, and LE90% is 90% of RMSE).

Table 4 Settings of DEM smoothing methods.

Table 5 Bankfull discharges in the upstream and downstream parts of the selected river with different Manning's roughness coefficients.

Fig. 1

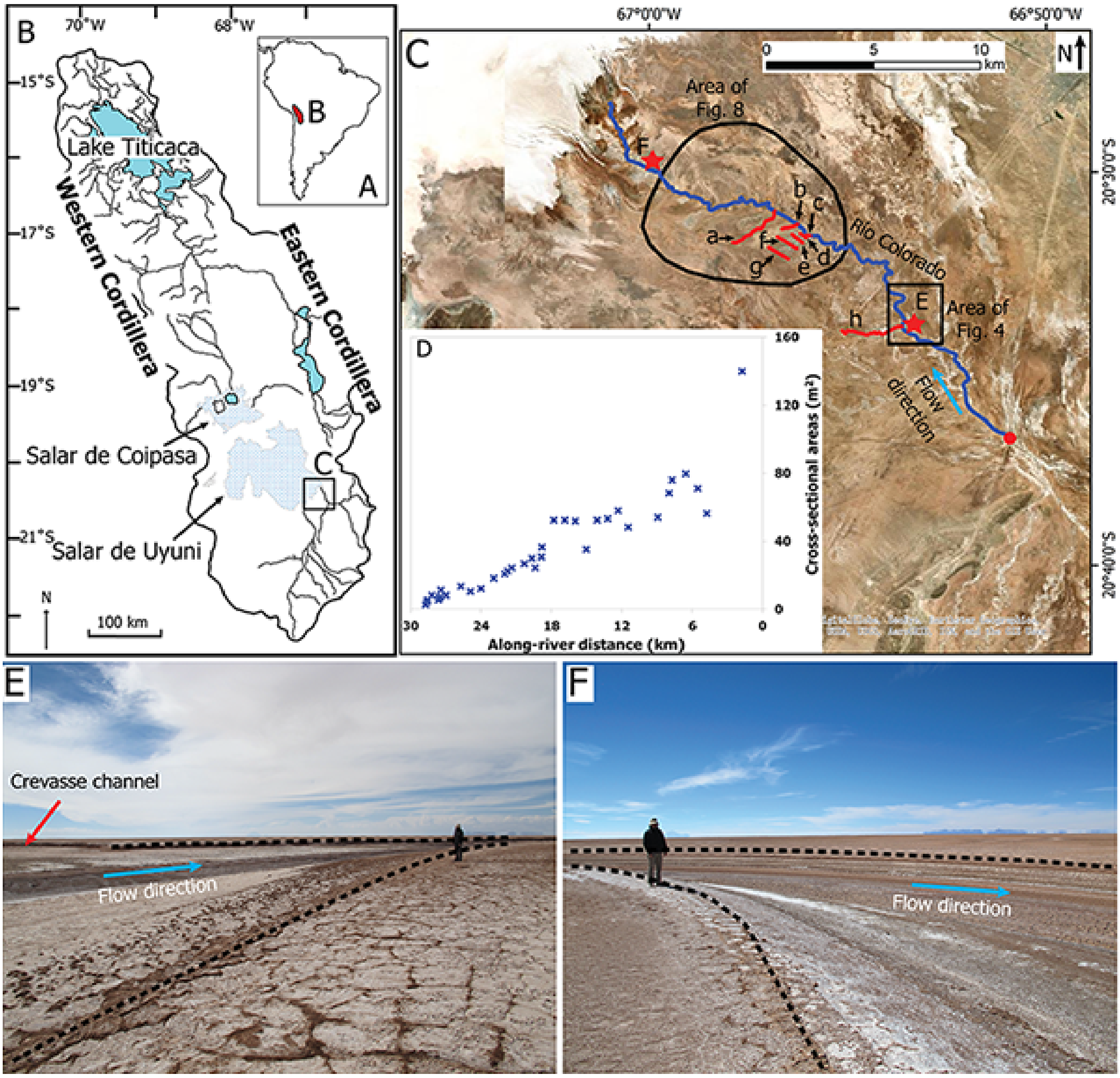

B
70°W
68°W
15°S
17°S
19°S
21°S
Lake Titicaca
Western Cordillera
Eastern Cordillera
Salar de Coipasa
Salar de Uyuni
C
N
100 km
A
B
C
67°0'0"W
66°50'0"W
20°30'0"S
20°40'0"S
0
5
10
km
N
Area of
Fig. 8
F
a
b
c
d
e
f
g
h
Río Colorado
E
Area of
Fig. 4
Flow
direction
D
Cross-sectional areas (m²)
Along-river distance (km)
E
Crevasse channel
Flow direction
F
Flow direction

Fig. 2

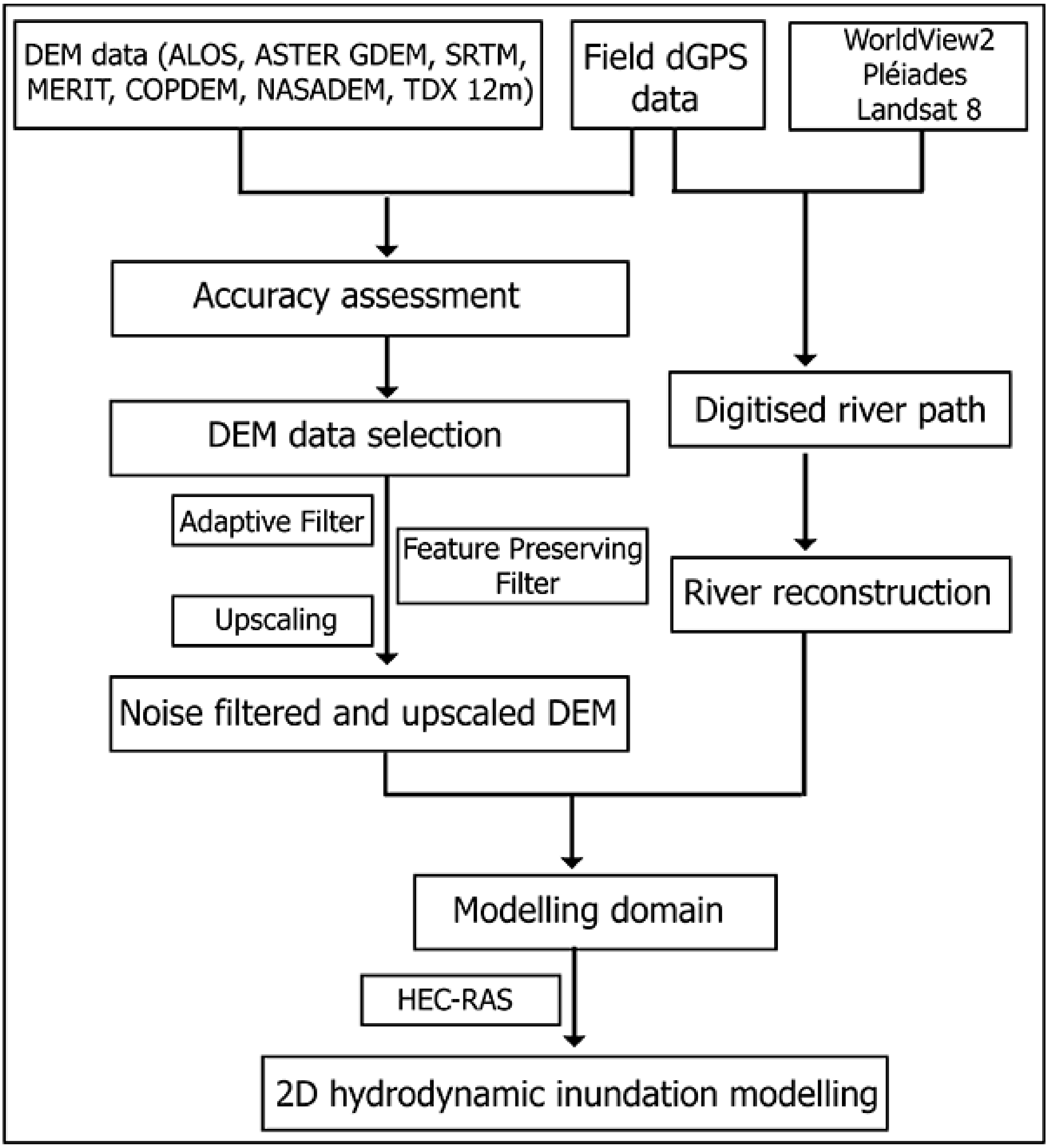
DEM data (ALOS, ASTER GDEM, SRTM, MERIT, COPDEM, NASADEM, TDX 12m)
Field dGPS data
WorldView2
Pléiades
Landsat 8
Accuracy assessment
Digitised river path
DEM data selection
Adaptive Filter
Feature Preserving Filter
Upscaling
River reconstruction
Noise filtered and upscaled DEM
Modelling domain
HEC-RAS
2D hydrodynamic inundation modelling

883 Fig. 3

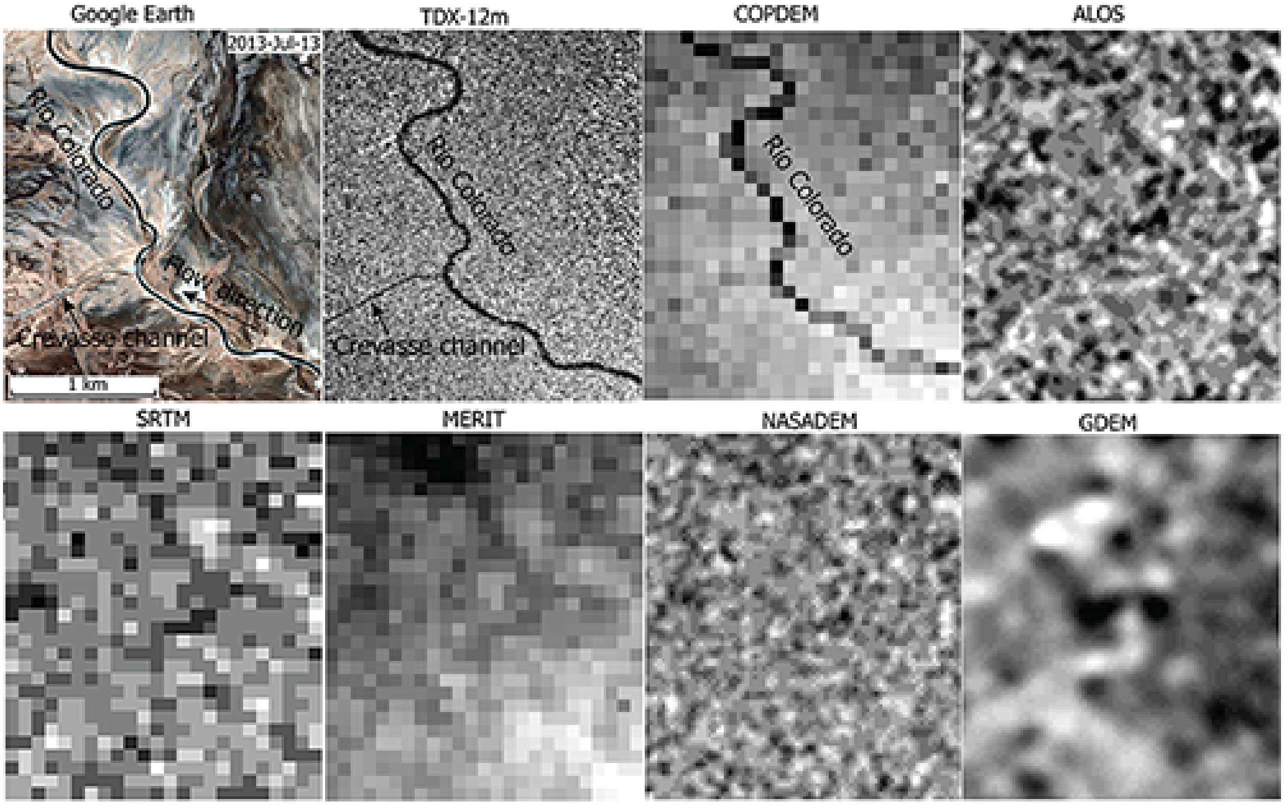

884

885

Fig. 4

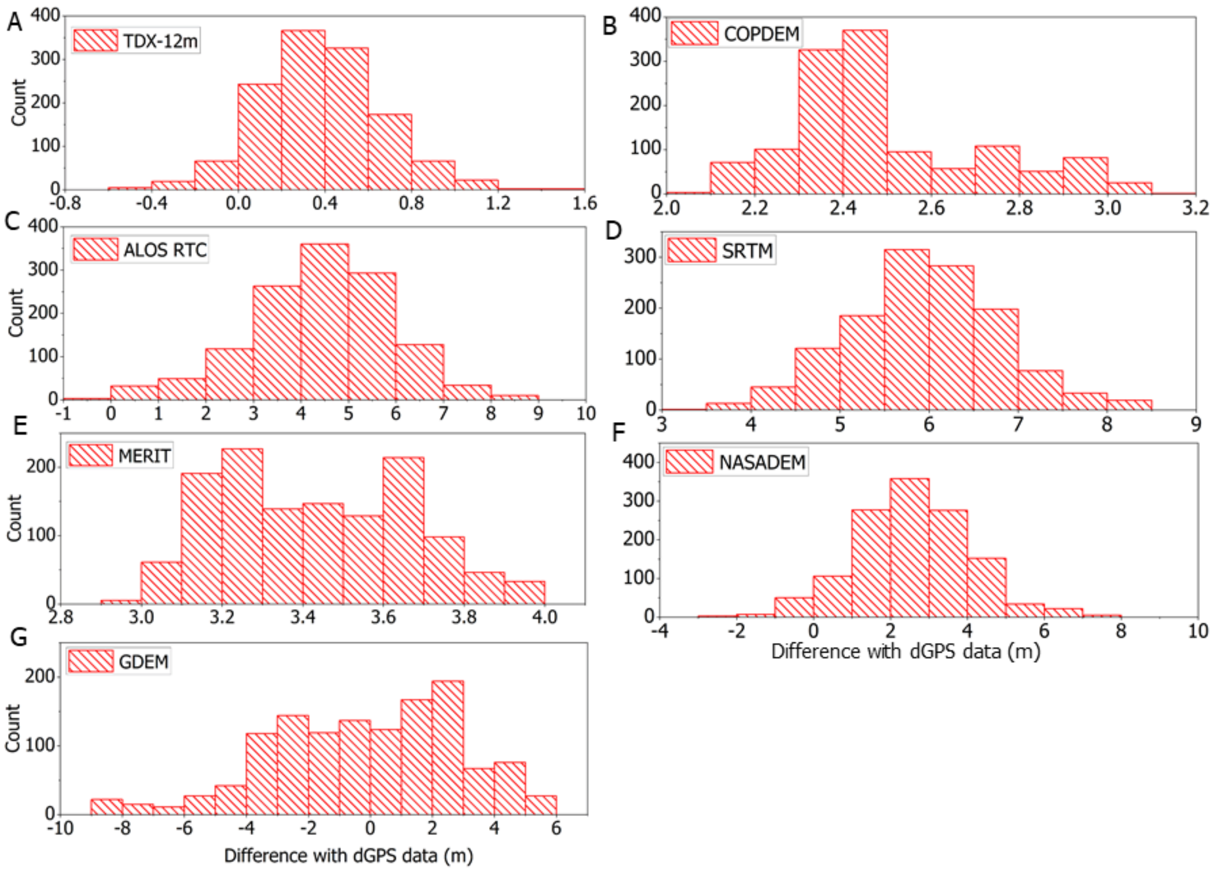
A
TDX-12m
B
COPDEM
C
ALOS RTC
D
SRTM
E
MERIT
F
NASADEM
G
GDEM
Count
Difference with dGPS data (m)

Fig. 5

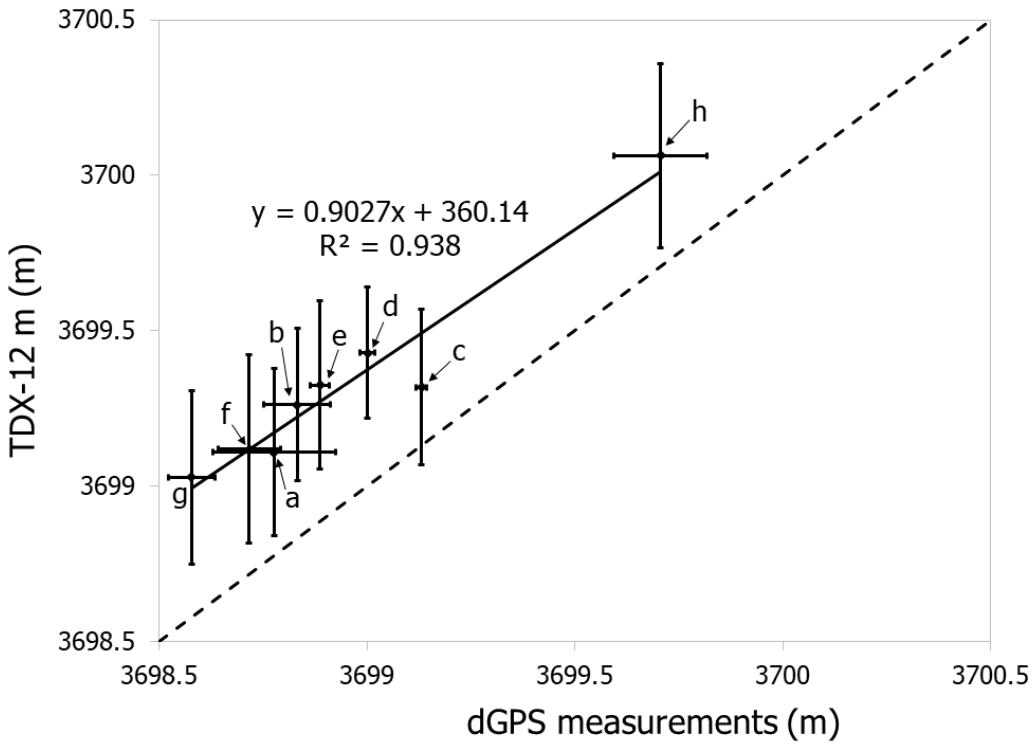
y = 0.9027x + 360.14
R² = 0.938
a
b
c
d
e
f
g
h
TDX-12 m (m)
dGPS measurements (m)
3698.5
3699
3699.5
3700
3700.5

Fig. 6

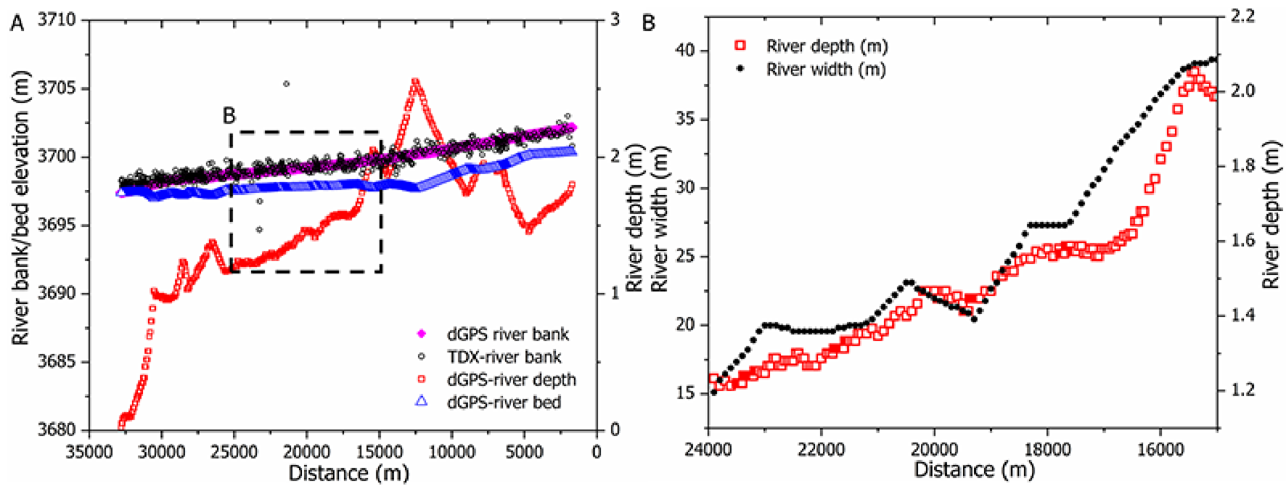
A
B
River bank/bed elevation (m)
Distance (m)
River depth (m)
River width (m)
dGPS river bank
TDX-river bank
dGPS-river depth
dGPS-river bed
River depth (m)
River width (m)
River depth (m)
Distance (m)

Fig. 7

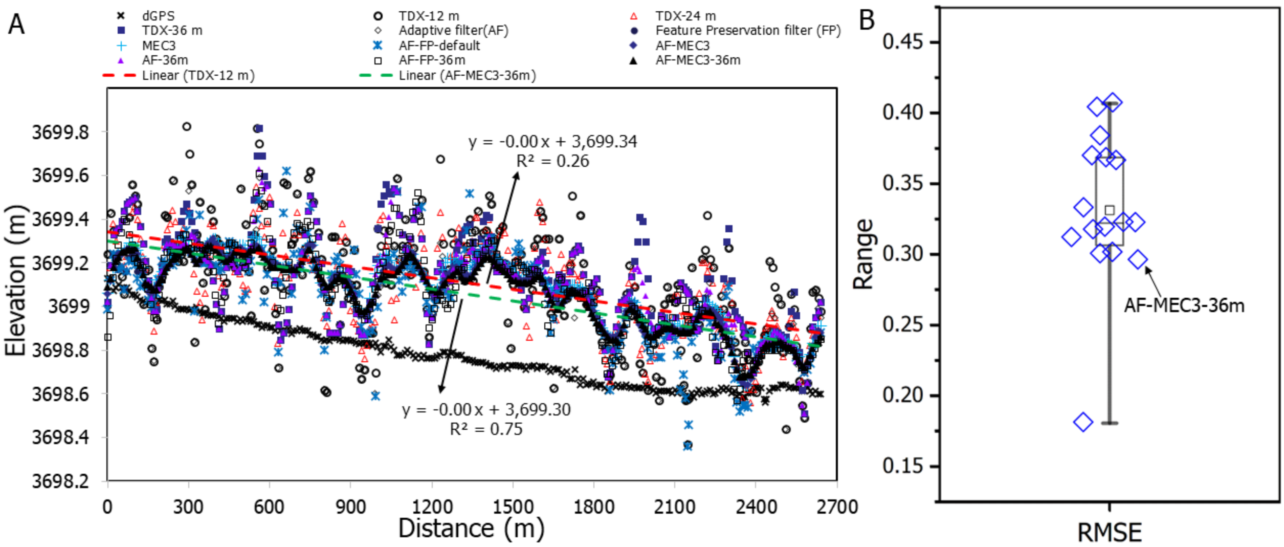
A
dGPS
TDX-36 m
MEC3
AF-36m
Linear (TDX-12 m)
TDX-12 m
Adaptive filter(AF)
AF-FP-default
AF-FP-36m
Linear (AF-MEC3-36m)
TDX-24 m
Feature Preservation filter (FP)
AF-MEC3
AF-MEC3-36m
y = -0.00 x + 3,699.34
R² = 0.26
y = -0.00 x + 3,699.30
R² = 0.75
Elevation (m)
Distance (m)
B
Range
AF-MEC3-36m
RMSE

Fig. 8

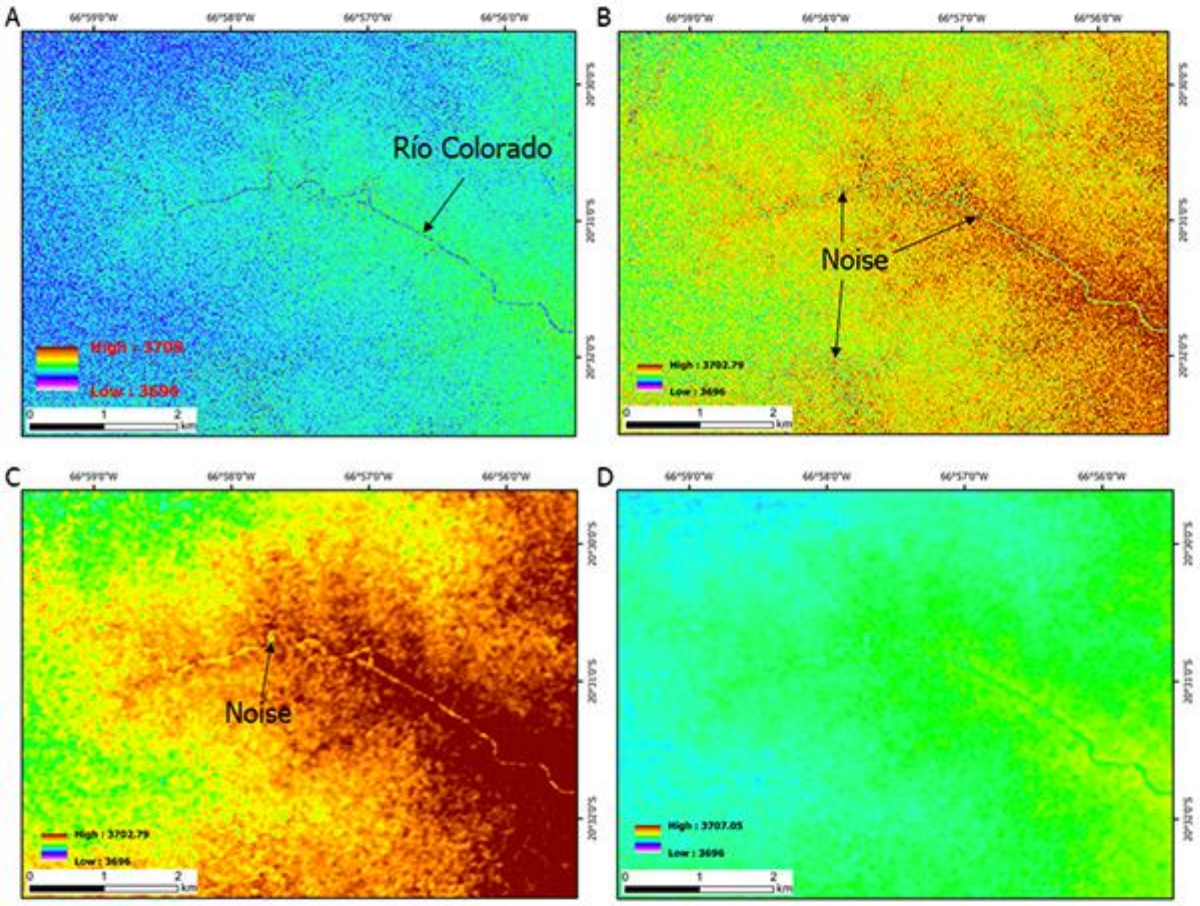
A
B
C
D
Río Colorado
Noise
Noise
High : 3708
Low : 3696
High : 3702.79
Low : 3696
High : 3702.79
Low : 3696
High : 3707.05
Low : 3696
0 1 2 km

Fig. 9

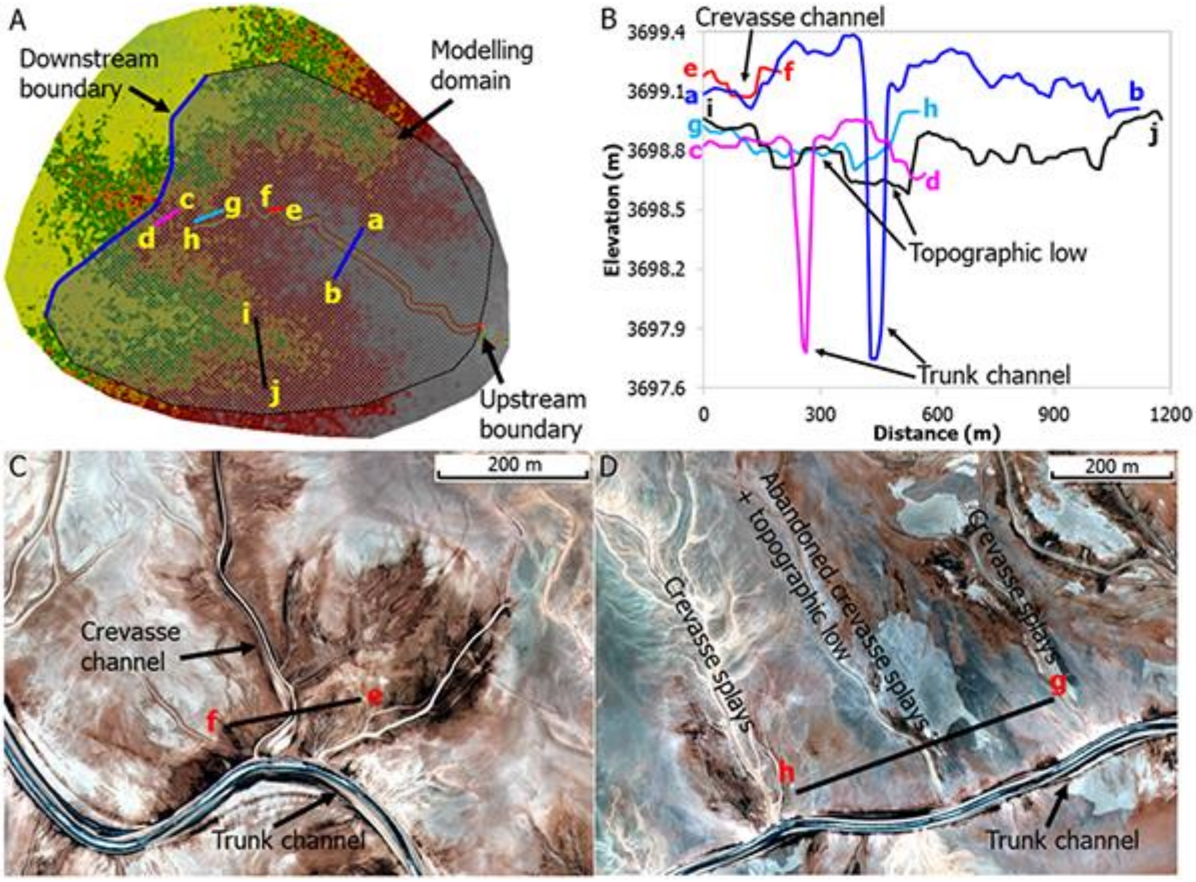

A
Downstream boundary
Modelling domain
Upstream boundary
a
b
c
d
e
f
g
h
i
j
B
Crevasse channel
Elevation (m)
3699.4
3699.1
3698.8
3698.5
3698.2
3697.9
3697.6
Topographic low
Trunk channel
0
300
600
900
1200
Distance (m)
C
200 m
Crevasse channel
Trunk channel
D
Abandoned crevasse splays + topographic low
Crevasse splays
Trunk channel

Fig. 10

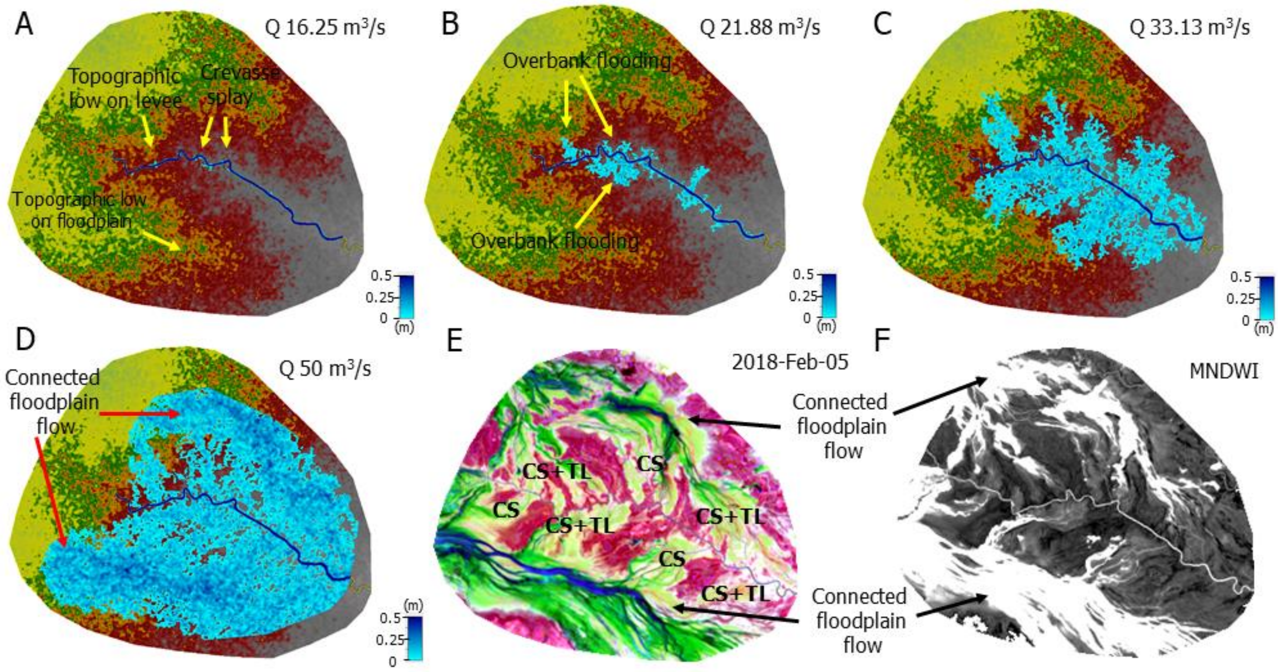

A
Q 16.25 m³/s
Topographic low on levee
Crevasse splay
Topographic low on floodplain
B
Q 21.88 m³/s
Overbank flooding
Overbank flooding
C
Q 33.13 m³/s
0.5
0.25
0
(m)
D
Q 50 m³/s
Connected floodplain flow
E
2018-Feb-05
CS+TL
CS
Connected floodplain flow
F
MNDWI
Connected floodplain flow

Table 1

Data	Catalog ID	Horizontal resolution (m)	Acquisition date	Vertical error
TDX-12 m	TDM1_DEM_04_S21W67	~12	05/01/2011	<2 m for low slope areas (<20%) 4 m for high slope areas (>20%; Rizzoli et al., 2017);
	TDM1_DEM_04_S21W68	~12	12/02/2011	90% linear error < 2 m (Wessel et al., 2018)
Copernicus DEM	DEM1_SAR_DGE_90_20110105T095417_20140822T100340_ADS_000000_5935	~90 m	05/01/2011	Derived from original TDX-DEM data
ALOS RTC (RT1)	AP_27132_FBS_F6760_RT1	~12.5	2011	Accuracies are reported only for the 5m dataset as an RMSE of 5m for horizontal and vertical (Takaku et al., 2014).
	AP_27132_FBS_F6770_RT1	~12.5		
SRTM	S21W067_dem	~30	2000	16 m (mission specification) Rodriguez et al., 2006); <10 m (Farr et al., 2007); 3.6 m (Berry et al., 2007)
	S21W068_dem			
MERIT	s25w070_dem	~30	2000	Derived from original telemetry data from the Shuttle Radar Topography Mission (SRTM) 58% <2 m (Yamazaki et al., 2017)
NASADEM	NASADEM_NC_s21w067	~30	2000	Derived from original telemetry data from the Shuttle Radar Topography Mission (SRTM)
	NASADEM_NC_s21w068	~30		
GDEM v3	ASTGTM_S21W067_dem	~30	2000	A global average vertical RMSE and SD of < 12 m (Tachikawa et al., 2011).
	ASTGTM_S21W068_dem	~30		

Table 2

Type	Catalog ID	Acq. date	Spatial resolution (m)	Avg. off nadir angle	Avg. target azimuth	Sensor
Worldview-02	10300100084D5600	09-Dec-10	0.49	13°	173°	WV02
Pléiades	DS_PHR1B_201307131443591_SE1_PX_W067S21_0310_02391	13-Jul-13	0.5	16°	33°	PHR1B
Landsat 8	LC82330742018036LGN00	05-Feb-18	30	NADIR	87°	OLI_TIRS

Table 3

	Crevasse splays							Main channel
	TDX-12 m	COPDEM	ALOS RTC	SRTM	MERIT	NASADEM	GDEM	TDX-12 m
ME	0.38	2.492	4.32	5.95	3.43	2.62	-0.13	0.09
MAE	0.4	2.492	4.32	5.95	3.43	2.67	2.5	0.33
RMSE	0.47	2.5	4.58	6.02	3.44	3.01	3.03	0.49
LE90%	0.43	2.25	4.11	5.41	3.1	2.71	2.72	0.44

Table 4

Adaptive filter	Feature-preserving DEM smoothing				
Filter kernel size	Filter kernel size	Maximum difference in normal vectors	Number of iterations	Maximum allowable absolute elevation change	Z conversion factor
11×11	11×11	15	3	3	1

Table 5

Manning's roughness	0.02		0.03		0.04		0.05	
Bankfull discharge (m^3/s)	Upstream reach	Downstream reach	Upstream reach	Downstream reach	Upstream reach	Downstream reach	Upstream reach	Downstream reach
	24.05	17.72	21.88	15.31	20	12.5	19.06	11.56